Hints of Growth Mechanism Left in Supercrystals

Heather A. Calcaterra,[1,2^] Cindy Y. Zheng, [2,3^] Soenke Seifert,[3^] Yudong Yao,[4] Yi Jiang,[4] Chad A. Mirkin[1,2,3*], Junjing Deng, [4*] Byeongdu Lee [4*]

*Email: CM(chadnano@northwestern.edu) , JD(junjingdeng@anl.gov) , BL(blee@anl.gov)

^ Equal contribution

*Corresponding authors

[1]Department of Chemical and Biological Engineering, Northwestern University, Evanston, IL, 60208, United States
[2]International Institute for Nanotechnology, Northwestern University, Evanston, Illinois 60208, United States
[3]Department of Chemistry, Northwestern University, Evanston, IL, 60208, United States
[4]X-ray Science Division, Advanced Photon Source, Argonne National Laboratory, Argonne, Illinois 60439, United States

Abstract

Supercrystals of DNA-functionalized nanoparticles are visualized in 3D using x-ray ptychographic tomography, and their reciprocal spaces are mapped with small angle x-ray scattering (SAXS) in order to better understand their internal defect structures. X-ray ptychographic tomography reveals various types of defects in an assembly which otherwise exhibits a single crystalline diffraction pattern. On average, supercrystals composed of smaller nanoparticles are smaller in size than supercrystals composed of larger particles. Additionally, supercrystals composed of small nanoparticles are typically aggregated into larger "necklace-like" structures. Within these larger structures, some but not all pairs of connected domains are coherent in their relative orientations. In contrast, supercrystals composed of larger nanoparticles with longer DNA ligands typically form larger, faceted crystals. The combination of these two complementary x-ray techniques reveal that the crystalline assemblies grow by aggregation of smaller assemblies followed by rearrangement of nanoparticles.

Keywords: Supercrystal, DNA, Colloid, Growth Mechanism, Ptychography, Tomography, X-ray Imaging

A thorough visualization of nanoscale materials structure is essential to both fundamental understanding of a material and its use in applications. Crystalline assemblies of colloidal nanoparticles, known as supercrystals, are a unique class crystalline structures because both the particle cores and crystal symmetries can be tuned independently, which in turn controls their resulting properties. In addition to their crystalline structures, which can be determined by well-established diffraction-based techniques, imperfections in these materials can have a strong impact on their electronic,[1, 2] magnetic, and optical properties,[3] as well as their performance in applications such as catalysis[4] and gas sorption. In addition, an understanding of crystal defects can provide valuable insights into their growth mechanisms.

Despite the interest in understanding and controlling the defect structures in supercrystals, traditional assembly methods such as slow drying[5] or ligand removal[6] typically have limited synthetic control over defect structures, as they do not provide straightforward handles for controlling the strength of the attractive interactions between particles. Generally, nanoparticles can form highly crystalline assemblies only when the strength of attractive interparticle interactions are relatively weak such that bound nanoparticles can reversibly bind and unbind under the experimental growth conditions, rearranging into thermodynamically-preferred lattice positions.[7] While there have been several attempts like ligand exchange[8] and solvent vapor annealing[9], it is still challenging to reconfigure the particle arrangement once a superlattice is formed.

To address these limitations, one strategy that provides an exceptional handle over the interactive forces between particles is using DNA as a bonding agent between particles.[10-12] Particles can be functionalized with dense shells of DNA designed with complementary regions that enable the particles to act as programmable atom equivalents (PAEs) and assemble, typically at room temperature. By controlling the sequence and length of DNA used, the interaction strength between resulting particles can be finely tuned. Furthermore, within a broad temperature range, typically designed to be slightly above room temperature, the DNA linker sticky ends can reversibly hybridize and dehybridize at comparable rates, providing an efficient error correction pathway that enables particle crystallization upon heat treatment. As a result, crystals grown using the DNA-mediated approach are often of superior quality, and this approach has been successfully applied to obtain faceted single-crystals for a wide range of systems.[13-15]

From many computer simulations[16] and indirect visualization techniques such as *in situ* SAXS,[17] it is now believed that supercrystals assembled with DNA grow not only through a classical nucleation and growth mechanism but also *via* rearrangement of amorphous aggregates[18] if the cohesive energy between particles is not too strong compared to the thermal energy.[19] Therefore, stronger interactions between the particles are anticipated to cause structural defects in DNA-assembled supercrystals. Relatedly, studies have shown that even supercrystals which appear as well-faceted single crystals can contain internal defects.[20-23] Direct observation of these structural defects, however, have rarely been made due to the lack of experimental techniques.

Typically, electron microscopy is used to image nanoparticle supercrystals. Transmission electron microscopy (TEM) can image the interior of crystals, providing information on their internal defect structures.[24, 25] However, TEM is limited by the shallow penetration depth of electrons, enabling imaging of only ~100 nm in depth, equating to just a few supercrystal planes. Scanning electron microscopy (SEM), by nature, provides only surface information, allowing visualization of defects that propagate to the surface of crystals. However, when combined with focused ion beam (FIB), known as FIB-SEM, it becomes capable of visualizing internal structures within assemblies.[26-28] This destructive technique allows for imaging larger volumes compared to TEM. However, its resolution perpendicular to the sample surface is limited to approximately 3 nm, and cutting artifacts can be potentially introduced to degrade the image quality depending on the characteristics of the ion/plasma beam. These imaging techniques typically require transfer of the supercrystals to the solid-state, which involves sample preparation techniques that deposit residual impurities such as salt crystals, obfuscating electron microscope images.[29, 30] For example, silica embedding, which is most commonly used to prepare DNA-assembled colloidal crystals for imaging, involves embedding the supercrystals in a thick silica matrix.[29] The thick silica shell could cause plural scattering in TEM, which can compromise both image contrast and spatial resolution.[31] In contrast, x-ray ptychography,[32] a coherent diffractive imaging technique, can be employed to image the internal structure of supercrystals with a spatial resolution similar to FIB-SEM in 3D when combined with computed tomography.[33] Thanks to weaker interactions of x-rays with materials compared to electrons, or the high penetration depth of x-rays, this technique could potentially enable imaging of colloidal crystals under environments including thick silica matrices or, ideally, under aqueous condition. Importantly, it shares the same data collection geometry with small angle x-ray scattering (SAXS), enabling the simultaneous collection of high-resolution

diffraction patterns. We utilized this combined x-ray imaging and scattering technique to visualize supercrystals formed by assembling gold nanoparticles with DNA.

Result and Discussion

In this work, nanoparticles of varying sizes (40-80 nm) were assembled into body-centered cubic (BCC) assemblies with two lengths of DNA, a 45 base "short DNA" and a 66 base "long DNA" (see Table S1 for sequences). The samples are designated with the code X-R*nn*, where X represents the length of DNA with S and L indicating short and long DNA, respectively, while *nn* represents the rounded radius of gold nanoparticles. Specifically, to synthesize each sample, two sets of gold nanoparticles were densely functionalized with 3'-propyl-thiol modified DNA anchor strands *via* a salt aging process.[34, 35] Linker strands were hybridized onto the anchor strands, exposing six-base single-stranded overhangs, known as sticky ends. The sticky ends on the two sets of particles are complementary to enable binding between the nanoparticles. Next, the two sets of nanoparticles were combined in buffer at room temperature, immediately forming aggregates. The aggregates were then heated above their melting temperature and cooled to room temperature at 0.1 ˚C/20 min, resulting in crystalline assemblies with sizes ranging from one micron to tens of microns. The crystal symmetries and domain sizes of the assemblies can be determined from solution SAXS data collected on the assemblies precipitated at the bottom of aqueous buffer solution in Eppendorf tubes. Figure 1 shows representative SAXS data from samples assembled with long DNA. As the gold particle size increases, the supercrystals exhibit sharper diffraction peaks, indicating larger domain size (Figure S1 shows azimuthally averaged 1D profiles). Notably, the sample L-R25, which has the smallest domain size, displays the fewest number of diffraction spots overlaid on diffraction rings. These systematically distributed spots are unexpected since smaller crystals typically result in a larger number of randomly oriented crystals, generating many randomly oriented spots or rings. Further, closer examination of the diffraction spots in Figure 1a reveals fiber symmetry around [110] (indexed in Figure S2), indicating that multiple supercrystals are oriented such that their (110) planes are parallel to one another. However, their respective spatial arrangement cannot be resolved from this solution SAXS data.

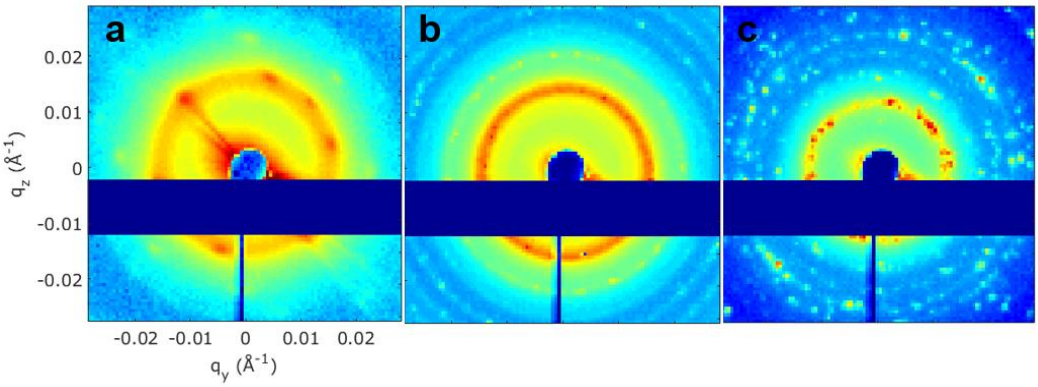

Figure 1. Solution SAXS data from aggregates of assemblies. Representative solution SAXS data from (a) L-R25, (b) L-R30, and (c) L-R40.

To visualize the supercrystals, assemblies were embedded in silica,[29] drop-casted onto a silicon nitride frame, and dried. X-ray ptychographic tomography was performed for the sample on the frame with similar procedures demonstrated in a previous study.[36] Reconstructed 2D projection images were fed into a computed tomography routine[37] to obtain 3D volumetric data with a voxel size of 18 nm. After each tomography scan, the focusing optics were removed and SAXS measurements were performed with a larger detector that covers higher q range. Then, the reciprocal space maps were constructed from SAXS data measured for the same range of rotation angles. This SAXS data on the dried samples became a reference to the ptychography reconstruction data and was used to determine the supercrystal orientation. Then, coordination of the volumetric data was converted to visualize the 3D data in *hkl* fractional coordinates. Figure 2 shows schematics of the experimental setup. The voxel size of the reconstructed volumetric data is 18 nm, which is about half the size of the smallest particles used in this work. Due to a missing wedge in the measurement (~ 60 ° angular range), there are fewer Fourier synthesis components in the x direction, or the direction of the beam, than other directions and thus, reconstructed electron densities are slightly elongated along the x direction. In addition, our prototype SAXS/ptychography setup used in this work has not yet been equipped with high resolution interferometers for precise sample positioning with respect to the focusing optics, resulting in compromised spatial resolution of tomograms.

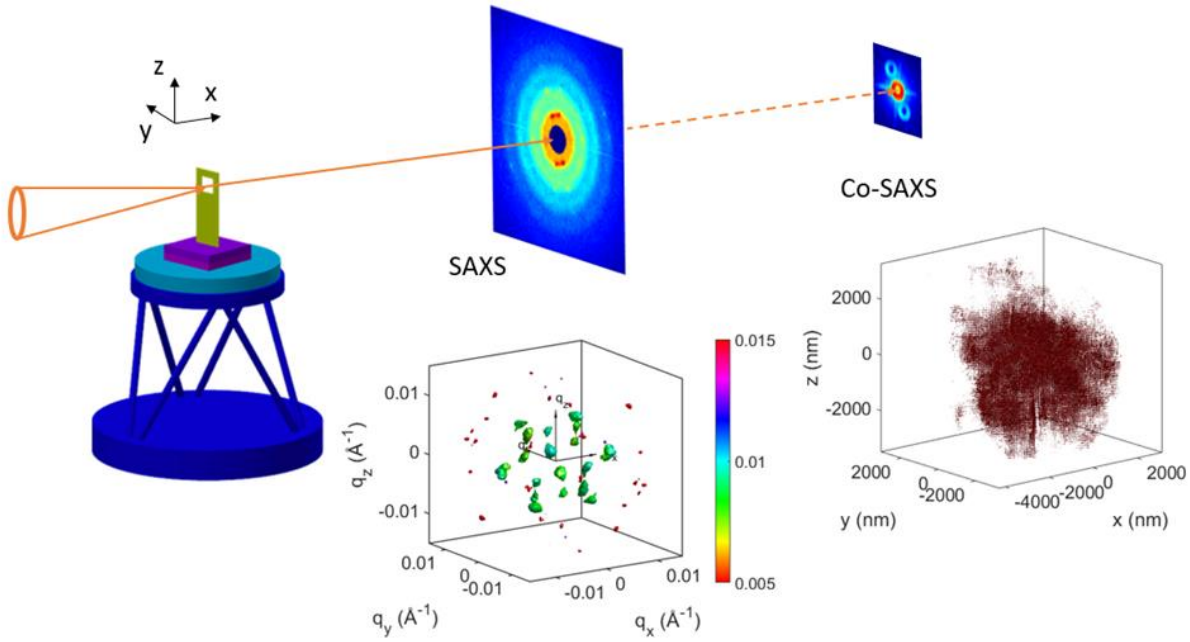

Figure 2. Schematic showing a typical x-ray ptychography set-up to measure supercrystals. The SAXS detector moves in and out of the beam for the measurement. The reciprocal space map and the tomogram of S-R40 are from SAXS and ptychographic tomography (or Coherent SAXS), respectively.

Table 1. Crystallographic data. Sample code: X-R*nn*, where X = S or L and *nn* = 25, 30, or 40. The estimated face-to-face distances in solution for samples with the short DNA (S) and the long DNA (L) are 23.8 and 34.5 nm, respectively. The radii of nanoparticles determined from SAXS for R25, R30, and R40 are 25.0, 29.2, and 41.0 nm, respectively. Ptychography and SAXS data were collected in the solid state through silica embedding and in solution without any processing, respectively. [a]Nearest neighbor distance. [b]Shortest distance between the surfaces of two nearest neighboring particles.

Method	**Sample**	**a (nm)**	**b (nm)**	**c (nm)**	α (deg)	β (deg)	γ (deg)	**NN distance[a] (nm)**	**Face-face distance[b] (nm)**
Ptycho	S-R25	64.1	64.2	63.5	90	90	90	55.4	5.4

		64.0 64.1	64.1 64.2	64.0 61.5	93 88	90 90	94 88	53.2 56.0	3.2 6.0
Ptycho	L-R25	77.3 71.7	76.5 71.7	75.8 71.7	90.2 90.0	90.0 90.0	90.6 90.0	66.0 62.1	16.0 12.1
Ptycho	S-R30	83.2 85.4	77.6 84.0	83.0 84.0	89 90	89 90	85 91	73.0 72.7	14.6 14.3
Ptycho	L-R30	96.2	94.9	94.5	89.8	90.3	91.1	81.9	23.5
Ptycho	S-R40	108.2	104.9	106.1	90.0	91.6	89.3	91.7	9.7
Ptycho	L-R40	108.8	113.8	115.8	91.3	90.1	88.6	97.7	15.7
SAXS	L-R25	100.9	-	-	-	-	-	87.4	35.8
SAXS	L-R30	107.0	-	-	-	-	-	91.9	33.5
SAXS	L-R40	130.7	-	-	-	-	-	113.2	31.2

Face-to-face distances calculated from solution SAXS profiles (shown in Figure S1) are close to the ideal value, 34.5 nm calculated from the complementary contact model.[11] In comparison to samples measured in solution, the dried samples, while embedded in silica, still have significantly compressed face-face distances, or interparticle gaps, up to half of the distances in solution. Upon silica embedding and the subsequent dehydration processes, duplexed DNA may change its conformation from B-form to A-form, causing a length decrease of up to 65%.[38, 39] In some silica embedded samples, tetragonal-like lattices are observed, which probably results from the non-complete space filling of silica. Despite the lattice deformation, all the samples retained body centered particle arrangements, proved by the intact reciprocal space map shown in Figure 2. All of the samples which utilize long DNA, namely L-R25, L-R30, and L-R40, show about 6~7 nm longer face-face distances than S-R25, S-R30, and S-R40, which utilize short DNA. This indicates that the lattice shrinks more or less proportionally to the length of the DNA. These sample preparation artifacts, namely lattice distortion and contraction, are primarily due to drying and can be avoided by employing cryo-cooling instead of silica embedding.[40] Apart from these artifacts caused by drying, our previous works on DNA-assembled supercrystals indicate that silica embedding does not bind nor fragment supercrystals.[13, 29, 40]

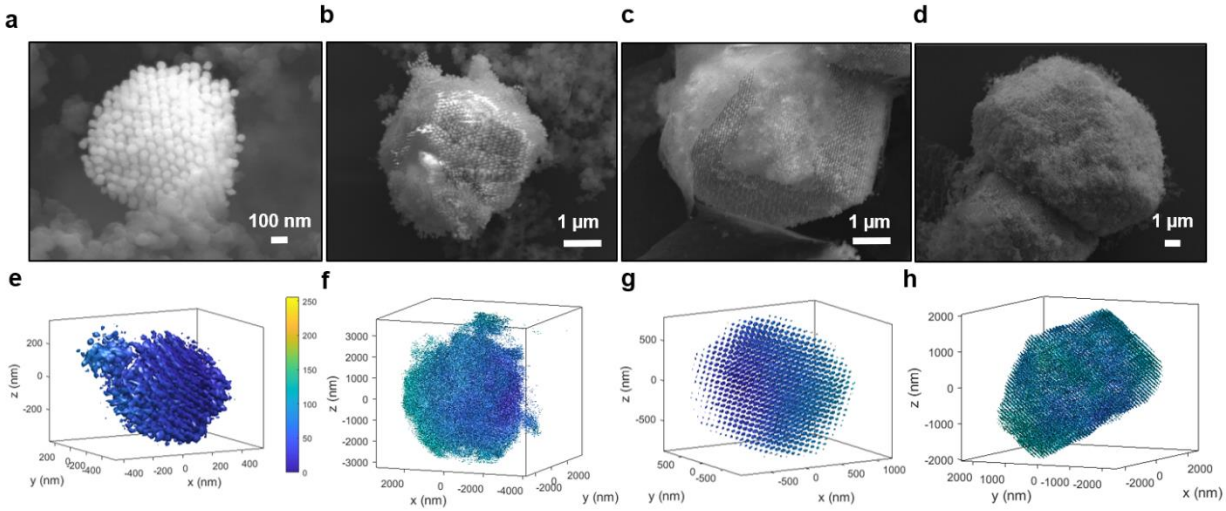

Figure 3. SEM and 3D x-ray ptychography reconstructions of colloidal crystals composed of spherical nanoparticles. Representative images of colloidal crystals engineered with DNA of (a) S-R30, (b) S-R40, (c) L-R30, and (d) L-R40. Isosurface plots of corresponding representative x-ray ptychographic tomograms of (e) S-R30, (f) S-R40, (g) L-R30, and (h) L-R40. 3D views are available as movie files (SI Movies).

SEM and x-ray tomograms show representative supercrystals that contain high levels of surface ordering of nanoparticles in all samples. While the SEM images reveal the supercrystals' exterior shapes and a small number of their surface layers, the ptycho-tomography data brings in clear, multidimensional images of the supercrystals,(Supplementary Movies) fully resolving their morphologies and internal defect structures, owing to the high Z-contrast between silica and the gold nanoparticles. From the SEM images and x-ray ptycho-tomograpy data, as well as solution SAXS (Figures 1 and S1), we observed that the sizes of the supercrystals increase with the particle size (Figure 3)Figure 3 regardless of the length of DNA. More subtly, the length of DNA also impacts the quality of obtained supercrystals. From the SEM images, supercrystals assembled with long DNA strands (L-R30 and L-R40) show better-faceted exteriors compared to those utilizing short DNA (S-R30 and S-R40) relative to the same core size. Ptycho-tomography data indeed indicate that samples which utilize long DNA, namely L-R30 and L-R40, develop better-faceted surfaces, while S-R30 and S-R40 show attachment of smaller supercrystals on the mother supercrystal's surface. Some of the smaller daughter crystals possess the same crystal orientation

as their mother, for example, one in S-R30, and some don't, for example, one in S-R40 (Figure S4).

The projected tomography data along the crystallographic directions, shown in Figure 4, reveal substantial interior defects in all samples excluding L-R30. Close to the surface of the S-R40 supercrystal, an edge dislocation is observed (Figure 4a). Figure 4b shows a sub-section around the edge dislocation. In the [100], [111], and [011] views, one can see a line of the lattice is curved and shifted to the middle of two ideal lattice lines, while the shift is not noticeable in [1-11] view. This indicates that the particles shift toward [1-11] direction, which is one of their bonding directions. More interestingly, on the opposite side of curved direction, a line of particles is missing. It appears that a particle that lost a neighbor on (-) side pulled to (+) side where it still has a neighbor. With sufficient annealing, this kind of line defect could likely be annihilated, considering the same defect is not found in the middle of the supercrystal. Nonetheless, as a result of the defect, the particle cannot keep the ideal BCC coordination. The projected data reveals the presence of domain boundaries, where two neighboring domains are connected through arrays of particles that exhibit less developed crystalline ordering. For example, S-R30 shown in Figures 4c and d, consists of two distinct grains, separated by a boundary indicated by the arrow in Figure 4d. This observation may suggest that the growth of supercrystals occurs through the attachment of smaller crystals. Based on our previous drying experiments, we have found that the DNA-assembled superlattice maintains its original structure even after undergoing multiple dehydration and hydration cycles. Therefore, we believe that the silica embedding process would less likely cause the observed edge dislocations and domain boundaries, which require significant and collective breakage of DNA bonds and formation of new bonds, respectively.

The projected tomography data also present thermal displacement-like defects, or positional displacement, along one of <111> directions, which is observed as lines in the projection images and as non-equal (110) reflections in the reciprocal space map (Figure S4 and 5). The lattice distortion is also noticed from the distribution of brighter and darker regions in those projected images. Since the fuzzy and lower intensity in the projection indicates the presence of less coherent lattice, this may indicate the presence of local domains, where their crystallographic orientations are slightly deformed (Figure 4e-f and Figure S3). L-R40 shown in Figure 4eFigure 4 and f shows bright areas, which are however larger than those of S-R30 and S-R40. One may notice a slight splitting of lattice lines in Figure 4eFigure 4, but two domains contributing each

line are from two opposite ends of the supercrystals. Compared to aforementioned dislocations and domain boundaries, the observed thermal displacement and lattice distortion could be attributed to the sample preparation process, namely silica embedding. This argument is supported by the fact that L-R30, which exhibits minimal lattice contraction, shows almost no positional displacement of particles. This well faceted crystal, composed of binary DNA-particles, exhibits no Schottky or Frenkel defects in the middle of the crystal. Thus, these specific types of defects will not be further discussed in this work.

We hypothesize that the observed edge dislocations and domain boundaries form when smaller supercrystals merge during annealing and eventually take on the same orientation. The observed line defects could be attributed to incomplete annealing and a large energy cost associated with annihilating line defects for samples assembled with short DNA. As discussed already, supercrystals composed of the short DNA (S-R30 and S-R40) had considerably more defect regions at places that appear to be phase boundaries between two supercrystals, than those with the long DNA design, likely due to the susceptibility of such systems to kinetic traps. The higher density of defects in the systems with the short DNA linkers is likely due to a higher attractive potential in the short DNA system, which can inhibit oriented crystallization due to bound particles needing to detach and subsequently reorganize into their ideal coordination positions. It is already known that more flexible DNA strands reduce the presence of defect structures in supercrystals.[41] As described above, when the same length of DNA is used, we found that with larger particles, the size of supercrystals increases. Concerning the size of supercrystals, the particle size shows far more significant impact than the DNA length. This is related to the fact that the number of DNA chains in a unit cell increases with the increase of particle size due to the larger surface area. When a larger core is utilized, the aggregate melting temperature and crystallization temperature both increase.[40] Therefore, during the slow cooling process, systems of larger cores crystallize at higher temperature, where PAEs have faster dynamics. Faster dynamics allow faster annihilation of domain boundaries, which will be expedited with employing longer, or flexible, DNAs.[41]

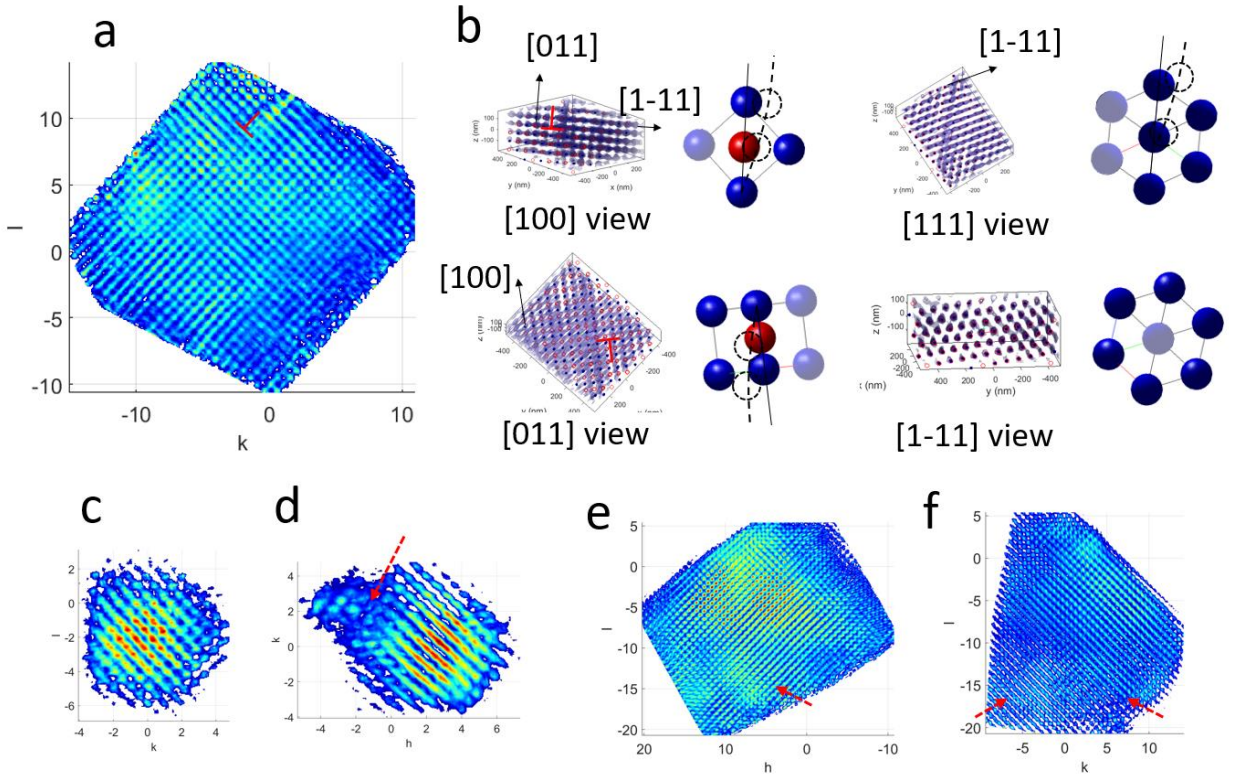

Figure 4. Projected densities along the crystallographic direction. (a) [100] projection of S-R40. (b) Sub-section around the edge dislocation in (a). Semi-transparent views of the isosurfaces are drawn along various view directions. The body center particles (red) are shifted to the dotted circle positions at the loss of their neighbors which are grayed out. (c) and (d) are projections of S-R30 along [100] and [001] directions, respectively. Dotted arrow in (d) denoted the boundary between a large and a small crystal. (e) and (f) are projections of L-R40 along [010] and [100] directions, respectively. The dotted arrow in (e) points two non-overlapping lines, each of which is from the opposite end sections of the supercrystals denoted by two arrows in (f).

Our proposed mechanism, the rearrangement of particles followed by attachment of small crystals, is more clearly observed for samples with smaller cores. Figure 5 shows ptycho-tomograms of the S-R25 and L-R25 made of the smallest core. In large area views (Figure 5a and c), both samples show many small crystals that are connected in random directions like a necklace,

and the size of each single domain is smaller than those with larger cores shown in Figure 3. Figure 5b and d show tomograms of selected regions. Connected crystalline domains are not always crystallographically correlated to one another, as seen in S-R25 (Figure 5b) between the yellow and red domains and in L-R25(Figure 5d). In the interdomain region, inevitable are point defects that could be annihilated upon further annealing.[16] In fact, within the same sample there was also a pair of correlated domains (yellow and blue) in Figure 5b. Consistent to the solution scattering data shown in Figure 1a, they are sharing the same (110) planes. Interestingly, all domains in the supercrystals are roughly the same size, indicating they have similar growth history. Observation of the aggregation of non-coherent domains supports our proposed mechanism that large supercrystals likely grow through random attachment of smaller supercrystals, which formed through nucleation and growth, and they may attach without crystallographic registration. As PAEs are still mobile at the elevated temperature, the two domains subsequently reorganize into a large, coherent supercrystal. This process is in contrast to Ostwald ripening, where smaller supercrystals dissolve in the presence of larger supercrystals and the particles from the smaller supercrystals deposit onto the larger supercrystals. When the crystallization temperature is too low, then the dehybridization kinetics becomes too slow and thus does not allow the rearrangement of the particles in the attached domains. Small crystals of S-R25 and L-R25 also support the finding that larger core size can yield a larger supercrystal because the lower curvature would allow higher population of DNA at the position of sticky ends and will increase the crystallization temperature.

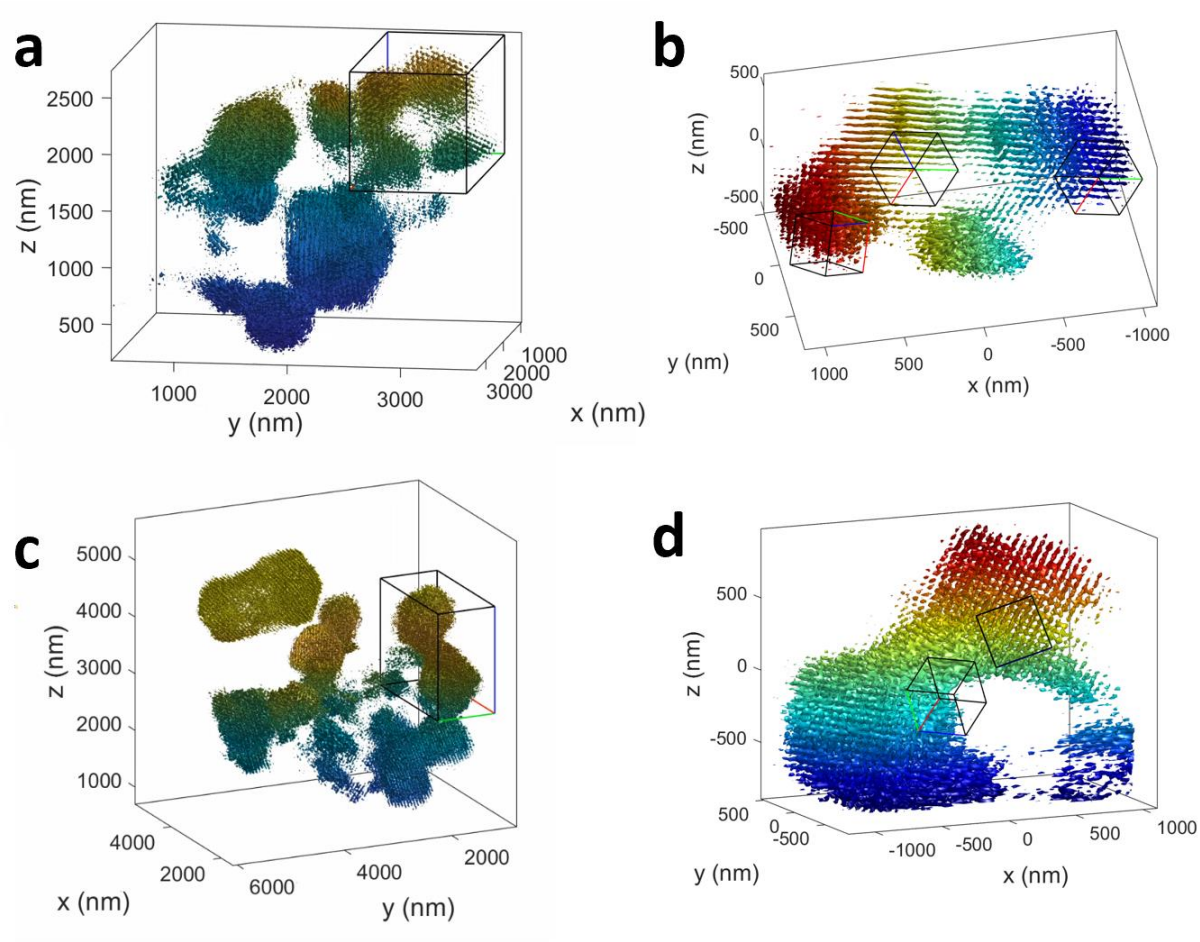

Figure 5. Ptychography reconstructions of supercrystals composed of small nanoparticles. Representative ptychography isosurface plot of assemblies from S-R25(a and b) and L-R25 (c and d). (b) enlarged view of the selected region in (a). Boxes in (b) and (d) are unit cells for domains where they are located. Although the red and yellow sections are uncorrelated, the blue section is coherent with respect to the yellow section. (d) enlarged view of the selected region in (c). The highlighted yellow and teal regions in (d) indicate different crystallographic attachment regions that are uncorrelated.

Conclusion

In summary, we utilized 3D x-ray ptychography to image the structure of a variety of DNA-assembled supercrystals. Thanks to high penetration power of x-ray, the ptychography data

revealed the complete structure of the crystals, enabling visualization of internal defects and their spatial distribution. Its yet limited resolution was compensated by the diffraction pattern analysis. This study revealed that although all of the supercrystals appear highly ordered from the outside, with well-defined crystal habits, their crystallinity and structure differed internally depending on particle core size as well as DNA ligand length utilized. Specifically, we found that supercrystals formed using larger particles and long DNA have a lower density of defects than supercrystals formed from smaller particles and shorter DNA. In addition, the presence of multiple connected domains in spherical superlattices revealed strong evidence for growth of supercrystals by aggregation of smaller crystals followed by rearrangement of nanoparticles. Our study indicates that DNAs grafted on nanoparticles lower the energy barrier in coherently merging small and independently nucleated and grown supercrystals and enables their sintering into a larger supercrystal.

Experimental Section

Supercrystal Synthesis

Gold nanoparticles were purchased from BBI Solutions. The oligonucleotides used in this work were synthesized on a solid-support MM48 synthesizer (BioAutomation) and the reagents utilized were purchased from Glen Research. Gold nanoparticles were functionalized with DNA by adding 3' propylthiolated anchor DNA and slowly increasing the salt concentration to 0.5 M NaCl to promote increased loading of DNA on the particle surface.[35] After functionalization, particles were washed to remove unreacted DNA. To assemble supercrystals, a stock solution was prepared by combining the functionalized nanoparticles with their linker strands to promote particle aggregation, heating the solution to 65 °C to dissociate the particles, and then slowly cooling the solution back down to room temperature at a rate of 0.1 °C per 10 min. Supercrystals were then embedded in a solid-state matrix of silica[29] and imaged using SEM (Hitachi SU-8030). Detailed methods can be found in the Supporting Information.

X-ray ptychography and Small Angle X-ray Scattering (SAXS)

Both x-ray ptychography and SAXS was performed at the 12-ID-C SAXS beamline of the Advanced Photon Source (APS) in Argonne National Laboratory. Two sets of vacuum flight tubes and detectors are used side-by-side. A Dectris Eiger 500K detector was placed at the downstream of about 5.57 m long vacuum tube for ptychography, and Dectris Pilatus 2M detector was placed at the downstream of about 2 m long vacuum tube for SAXS. Both sets were on a slide perpendicular to x-ray direction, and they were switched after each measurement. A coherent monochromatic x-ray beam at 10 keV energy was shaped to 80x100 (H x V) um^2 beam size with a set of beam defining slits and then focused by a Fresnel zone plate (FZP) with 70 nm outmost zone width. The sample was placed downstream of the focus position of the zone plate with an illumination size of ~1.2 μm. For 2D measurement of ptychographic projections, the sample was raster-scanned with 0.6 μm step size. For tomographic scan, the above 2D projection scans were collected at φ rotation angles ranging from -60 to 60 degree with 0.5 degree step. Ptychographic reconstruction was performed using phase retrieval software.[42] Because the phase part of the

reconstructed sample function has higher contrast in hard x-rays, only the obtained phase projections were used for computed tomography. In tomographic reconstruction, 2D projections were aligned to a common rotation axis using cross-correlation method and were then input into Tomopy software package to obtain tomogram using simultaneous iterative reconstruction technique (SIRT).[37] The tomographic result gave 3D distribution of the real part of the refractive index of the sample, δ, which is relative to electron density (n_e) through

$$\delta = \frac{n_e r_e \lambda^2}{2\pi},$$

where r_e is the classical electron radius and λ is x-ray wavelength.

For SAXS measurement, the FZP, the order sorting aperture (OSA), and the beamstop were translated out, and thus full 80x100 (H x V) um^2 beam was used with an exposure time of 5 seconds for the same φ angle range. From these SAXS diffraction patterns, the reciprocal space of the sample was mapped. SAXS patterns can also be calculated from the reconstructed tomogram. This process essentially desmears the beam shape due to a FZP from each coherent diffraction image. For samples of multi-domains, 3D SAXS patterns from each domain were calculated and used for the crystal orientation analysis.

Acknowledgement

This material is based upon work supported by the Air Force Office of Scientific Research award FA9550-17-1-0348 and the Sherman Fairchild Foundation, Inc. C. Zheng acknowledges support by the U.S. Department of Energy, Office of Science, Office of Workforce Development for Teachers and Scientists, Office of Science Graduate Student Research (SCGSR) program. The SCGSR program is administered by the Oak Ridge Institute for Science and Education (ORISE) for the DOE. ORISE is managed by ORAU under contract number DE-SC0014664. Any opinions, findings, and conclusions or recommendations expressed in this material are those of the authors and do not necessarily reflect the views of DOE, ORAU, or ORISE. H. Calcaterra acknowledges support by the National Science Foundation Graduate Research Fellowship Program grant (DGE-1842165). This research used resources of the Advanced Photon Source, a U.S. Department of Energy (DOE) Office of Science User Facility, operated for the DOE Office of Science by Argonne National Laboratory under Contract No. DE-AC02-06CH11357. This work made use

of the EPIC facility of Northwestern University's NU*ANCE* Center, which receives support from the Soft and Hybrid Nanotechnology Experimental (SHyNE) Resource (NSF ECCS-1542205); the MRSEC program (NSFDMR-1121262) at the Materials Research Center; the International Institute for Nanotechnology (IIN) and the State of Illinois, through the IIN. This research was supported in part by the National Science Foundation under Grant No. NSF PHY-1748958.

Supporting Information

Additional details of materials and methods, solution SAXS data, reciprocal space maps, and simulated models and their calculated reciprocal space map (PDF); and movies of the reconstructed volumetric data (movie files)

Author contribution

CZ and HC synthesized samples and performed SEM imaging, CZ, HC, SS, YY, JD, and BL performed x-ray experiments. SS, JD, and BL developed x-ray setups. YJ, JD and BL analyzed x-ray data. CM and BL overviewed the project.

References

(1) Jia, Y.; Jiang, K.; Wang, H.; Yao, X. The Role of Defect Sites in Nanomaterials for Electrocatalytic Energy Conversion. *Chem* **2019**, *5*, 1371-1397.
(2) Gubicza, J. Defect Structure in Low Stacking Fault Energy Nanomaterials. In *Defect Structure and Properties of Nanomaterials*, Elsevier: 2017; pp 95-119.
(3) Takeoka, Y. Stimuli-Responsive Opals: Colloidal Crystals and Colloidal Amorphous Arrays for Use in Functional Structurally Colored Materials. *J. Mater. Chem. C* **2013**, *1*, 6059.
(4) Xiong, J.; Di, J.; Xia, J.; Zhu, W.; Li, H. Surface Defect Engineering in 2d Nanomaterials for Photocatalysis. *Adv. Funct. Mater.* **2018**, *28*, 1801983.
(5) Rabani, E.; Reichman, D. R.; Geissler, P. L.; Brus, L. E. Drying-Mediated Self-Assembly of Nanoparticles. *Nature* **2003**, *426*, 271-274.
(6) Si, K. J.; Chen, Y.; Shi, Q.; Cheng, W. Nanoparticle Superlattices: The Roles of Soft Ligands. *Advanced science (Weinheim, Baden-Wurttemberg, Germany)* **2017**, *5*, 1700179-1700179.

(7) Lin, M. Y.; Lindsay, H. M.; Weitz, D. A.; Ball, R. C.; Klein, R.; Meakin, P. Universality in Colloid Aggregation. *Nature* **1989**, *339*, 360-362.
(8) Weidman, M. C.; Yager, K. G.; Tisdale, W. A. Interparticle Spacing and Structural Ordering in Superlattice Pbs Nanocrystal Solids Undergoing Ligand Exchange. *Chem. Mater.* **2015**, *27*, 474-482.
(9) Wang, Y.; Chen, J.; Zhu, C.; Zhu, B.; Jeong, S.; Yi, Y.; Liu, Y.; Fiadorwu, J.; He, P.; Ye, X. Kinetically Controlled Self-Assembly of Binary Polymer-Grafted Nanocrystals into Ordered Superstructures Via Solvent Vapor Annealing. *Nano Lett.* **2021**, *21*, 5053-5059.
(10) Mirkin, C. A.; Letsinger, R. L.; Mucic, R. C.; Storhoff, J. J. A DNA-Based Method for Rationally Assembling Nanoparticles into Macroscopic Materials. *Nature* **1996**, *382*, 607-609.
(11) Macfarlane, R. J.; Lee, B.; Jones, M. R.; Harris, N.; Schatz, G. C.; Mirkin, C. A. Nanoparticle Superlattice Engineering with DNA. *Science* **2011**, *334*, 204-208.
(12) Laramy, C. R.; O'Brien, M. N.; Mirkin, C. A. Crystal Engineering with DNA. *Nat. Rev. Mater.* **2019**, *4*, 201-224.
(13) Auyeung, E.; Li, T. I. N. G.; Senesi, A. J.; Schmucker, A. L.; Pals, B. C.; de la Cruz, M. O.; Mirkin, C. A. DNA-Mediated Nanoparticle Crystallization into Wulff Polyhedra. *Nature* **2013**, *505*, 73-77.
(14) Seo, S. E.; Girard, M.; Olvera de la Cruz, M.; Mirkin, C. A. Non-Equilibrium Anisotropic Colloidal Single Crystal Growth with DNA. *Nat. Commun.* **2018**, *9*, 4558-4558.
(15) O'Brien, M. N.; Lin, H.-X.; Girard, M.; Olvera de la Cruz, M.; Mirkin, C. A. Programming Colloidal Crystal Habit with Anisotropic Nanoparticle Building Blocks and DNA Bonds. *J. Am. Chem. Soc.* **2016**, *138*, 14562-14565.
(16) Knorowski, C.; Travesset, A. Dynamics of DNA-Programmable Nanoparticle Crystallization: Gelation, Nucleation and Topological Defects. *Soft Matter* **2012**, *8*, 12053-12059.
(17) Macfarlane, R. J.; Lee, B.; Hill, H. D.; Senesi, A. J.; Seifert, S.; Mirkin, C. A. Molecular Recognition and Self-Assembly Special Feature: Assembly and Organization Processes in DNA-Directed Colloidal Crystallization. *Proc. Natl. Acad. Sci. U.S.A.* **2009**, *106*, 10493-10498.
(18) Dai, W.; Kumar, S. K.; Starr, F. W. Universal Two-Step Crystallization of DNA-Functionalized Nanoparticles. *Soft Matter* **2010**, *6*, 6130-6135.
(19) Macfarlane, R. J.; Thaner, R. V.; Brown, K. A.; Zhang, J.; Lee, B.; Nguyen, S. T.; Mirkin, C. A. Importance of the DNA "Bond" in Programmable Nanoparticle Crystallization. *Proc. Natl. Acad. Sci. U.S.A.* **2014**, *111*, 14995-15000.
(20) Rupich, S. M.; Shevchenko, E. V.; Bodnarchuk, M. I.; Lee, B.; Talapin, D. V. Size-Dependent Multiple Twinning in Nanocrystal Superlattices. *J. Am. Chem. Soc.* **2010**, *132*, 289-296.
(21) Zhuang, J.; Wu, H.; Yang, Y.; Cao, Y. C. Supercrystalline Colloidal Particles from Artificial Atoms. *J. Am. Chem. Soc.* **2007**, *129*, 14166-14167.
(22) Shabalin, A. G.; Meijer, J. M.; Dronyak, R.; Yefanov, O. M.; Singer, A.; Kurta, R. P.; Lorenz, U.; Gorobtsov, O. Y.; Dzhigaev, D.; Kalbfleisch, S.; et al. Revealing Three-Dimensional Structure of an Individual Colloidal Crystal Grain by Coherent X-Ray Diffractive Imaging. *Phys. Rev. Lett.* **2016**, *117*, 138002.
(23) Lazarev, S.; Besedin, I.; Zozulya, A. V.; Meijer, J.-M.; Dzhigaev, D.; Gorobtsov, O. Y.; Kurta, R. P.; Rose, M.; Shabalin, A. G.; Sulyanova, E. A.; et al. Ptychographic X-Ray Imaging of Colloidal Crystals. *Small* **2018**, *14*, 1702575.
(24) Zanaga, D.; Bleichrodt, F.; Altantzis, T.; Winckelmans, N.; Palenstijn, W. J.; Sijbers, J.; de Nijs, B.; van Huis, M. A.; Sánchez-Iglesias, A.; Liz-Marzán, L. M.; et al. Quantitative 3d Analysis of Huge Nanoparticle Assemblies. *Nanoscale* **2016**, *8*, 292-299.
(25) Wang, D.; Dasgupta, T.; van der Wee, E. B.; Zanaga, D.; Altantzis, T.; Wu, Y.; Coli, G. M.; Murray, C. B.; Bals, S.; Dijkstra, M.; et al. Binary Icosahedral Clusters of Hard Spheres in Spherical Confinement. *Nat. Phys.* **2021**, *17*, 128-134.
(26) van der Hoeven, J. E. S.; van der Wee, E. B.; de Winter, D. A. M.; Hermes, M.; Liu, Y.; Fokkema, J.; Bransen, M.; van Huis, M. A.; Gerritsen, H. C.; de Jongh, P. E.; et al. Bridging the Gap: 3d Real-Space Characterization of Colloidal Assemblies Via Fib-Sem Tomography. *Nanoscale* **2019**, *11*, 5304-5316.

(27) Michelson, A.; Minevich, B.; Emamy, H.; Huang, X.; Chu, Y. S.; Yan, H.; Gang, O. Three-Dimensional Visualization of Nanoparticle Lattices and Multimaterial Frameworks. *Science* **2022**, *376*, 203-207.
(28) Lyu, J.; Chaâbani, W.; Modin, E.; Chuvilin, A.; Bizien, T.; Smallenburg, F.; Impéror-Clerc, M.; Constantin, D.; Hamon, C. Double-Lattice Packing of Pentagonal Gold Bipyramids in Supercrystals with Triclinic Symmetry. *Adv. Mater.* **2022**, *34*, 2200883.
(29) Auyeung, E.; Macfarlane, R. J.; Choi, C. H. J.; Cutler, J. I.; Mirkin, C. A. Transitioning DNA-Engineered Nanoparticle Superlattices from Solution to the Solid State. *Adv. Mater.* **2012**, *24*, 5181-5186.
(30) Oh, T.; Park, S. S.; Mirkin, C. A. Stabilization of Colloidal Crystals Engineered with DNA. *Adv. Mater.* **2018**, *31*, 1805480.
(31) Groves, T. Thick Specimens in the Cem and Stem. Resolution and Image Formation. *Ultramicroscopy* **1975**, *1*, 15-31.
(32) Pfeiffer, F. X-Ray Ptychography. *Nat. Photonics* **2017**, *12*, 9-17.
(33) Dierolf, M.; Menzel, A.; Thibault, P.; Schneider, P.; Kewish, C. M.; Wepf, R.; Bunk, O.; Pfeiffer, F. Ptychographic X-Ray Computed Tomography at the Nanoscale. *Nature* **2010**, *467*, 436-439.
(34) Hurst, S. J.; Hill, H. D.; Macfarlane, R. J.; Wu, J.; Dravid, V. P.; Mirkin, C. A. Synthetically Programmable DNA Binding Domains in Aggregates of DNA-Functionalized Gold Nanoparticles. *Small* **2009**, *5*, 2156-2161.
(35) Hurst, S. J.; Lytton-Jean, A. K. R.; Mirkin, C. A. Maximizing DNA Loading on a Range of Gold Nanoparticle Sizes. *Anal. Chem.* **2006**, *78*, 8313-8318.
(36) Deng, J.; Lo, Y. H.; Gallagher-Jones, M.; Chen, S.; Pryor, A., Jr.; Jin, Q.; Hong, Y. P.; Nashed, Y. S. G.; Vogt, S.; Miao, J.; et al. Correlative 3d X-Ray Fluorescence and Ptychographic Tomography of Frozen-Hydrated Green Algae. *Sci. Adv.* **2018**, *4*, eaau4548-eaau4548.
(37) Gürsoy, D. a.; De Carlo, F.; Xiao, X.; Jacobsen, C. Tomopy: A Framework for the Analysis of Synchrotron Tomographic Data. *Journal of synchrotron radiation* **2014**, *21*, 1188-1193.
(38) Radha, B.; Senesi, A. J.; O'Brien, M. N.; Wang, M. X.; Auyeung, E.; Lee, B.; Mirkin, C. A. Reconstitutable Nanoparticle Superlattices. *Nano Lett.* **2014**, *14*, 2162-2167.
(39) Sumi, H.; Ohta, N.; Sekiguchi, H.; Harada, S.; Ujihara, T.; Tsukamoto, K.; Tagawa, M. Two-Step Nanoparticle Crystallization Via DNA-Guided Self-Assembly and the Nonequilibrium Dehydration Process. *Cryst. Growth Des.* **2021**, *21*, 4506-4515.
(40) Lee, S.; Calcaterra, H. A.; Lee, S.; Hadibrata, W.; Lee, B.; Oh, E.; Aydin, K.; Glotzer, S. C.; Mirkin, C. A. Shape Memory in Self-Adapting Colloidal Crystals. *Nature* **2022**, *610*, 674-679.
(41) Senesi, A. J.; Eichelsdoerfer, D. J.; Brown, K. A.; Lee, B.; Auyeung, E.; Choi, C. H. J.; Macfarlane, R. J.; Young, K. L.; Mirkin, C. A. Oligonucleotide Flexibility Dictates Crystal Quality in DNA-Programmable Nanoparticle Superlattices. *Adv. Mater.* **2014**, *26*, 7235-7240.
(42) Wakonig, K.; Stadler, H.-C.; Odstrčil, M.; Tsai, E. H. R.; Diaz, A.; Holler, M.; Usov, I.; Raabe, J.; Menzel, A.; Guizar-Sicairos, M. Ptychoshelves, a Versatile High-Level Framework for High-Performance Analysis of Ptychographic Data. *J. Appl. Crystallogr.* **2020**, *53*, 574-586.

TOC

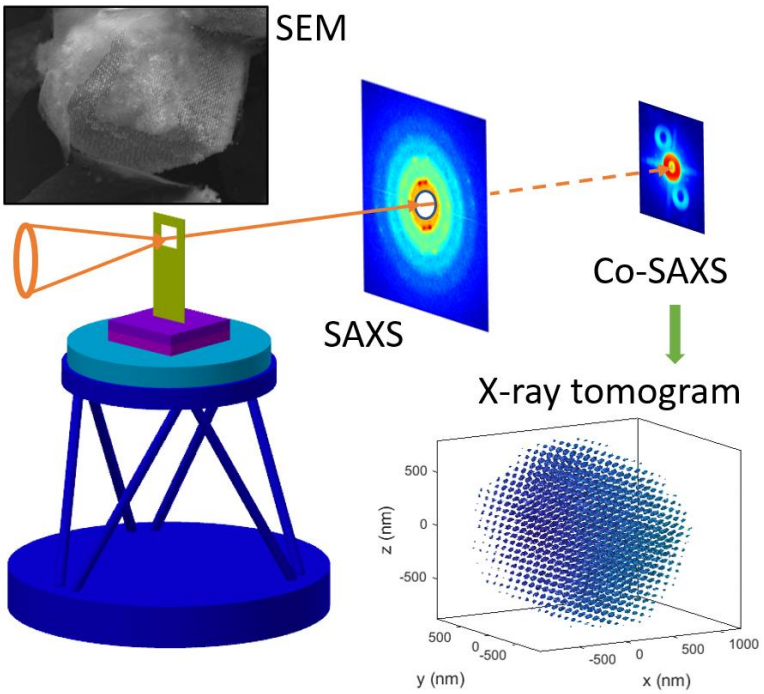
SEM
SAXS
Co-SAXS
X-ray tomogram
500
0
-500
z (nm)
500
0
-500
y (nm)
-500
0
500
1000
x (nm)